LAWRENCE
LIVERMORE
NATIONAL
LABORATORY

UCRL-JRNL-220120

Simultaneous interferometric optical-figure characterizations for two optical elements in series: Proposition of an unconventional numerical integration scheme

D.-H. Gwo

March 24, 2006

Optical Engineering

Title:

Simultaneous interferometric optical-figure characterizations for two optical elements in series: Proposition of an unconventional numerical integration scheme

Author:

Dz-Hung Gwo

Affiliation:

Lawrence Livermore National Laboratory

Livermore, CA 94550

Mailing Address: Jason Gwo, L-460, Lawrence Livermore National Laboratory, 7000 East Ave., Livermore, CA 94550

Telephone: (925) 422-8334

Fax: N/A

Email address: gwo1@llnl.gov

Simultaneous interferometric optical-figure characterizations for two optical elements in series: Proposition of an unconventional numerical integration scheme

Abstract:

The article proposes a scheme to break a catch-22 loop in an optical-figure/wavefont measurement. For instance, to measure the tilt-independent optical-figure of a nominal optical flat at cryogenic temperatures, it requires a cryogenic dewar-window system for a Fizeau interferometer outside the dewar to see through. The issue is: how to calibrate *in situ* the window system using the yet-to-be-calibrated nominal optical flat, and *vice versa*, in only one cryogenic cooldown? The proposition includes: a) interferometric phase-map measurements with the test piece slightly offset in different transverse directions, and b) for synthesizing the 2-dimentional WDF, an unconventional numerical scheme starting with 1-dimentional bi-direction integration. The numerical scheme helps minimize the non-uniformity in integrated noise-power distribution that results from integrating data, and thus the associated uncorrelated random noise, from raw phase-maps. The numerical scheme represents a new concept specifically for integrating noise-carrying *experimental* data.

Subject terms:

cryogenics, dewar window, Fizeau interferometry, optical wavefront, optimization, least-squares, uncorrelated random noise, numerical integration.

1. BACKGROUND

The article proposes a scheme to break a catch-22 loop in an optical-figure/wavefont measurement. For instance, to measure the tilt-independent optical-figure of a nominal optical flat at cryogenic temperatures, it requires a cryogenic dewar-window system for a Fizeau interferometer outside the dewar to see through. "For description of Fizeau interferometry, see Reference 1." The issue to be addressed is: how to calibrate *in situ* the window system using the yet-to-be-calibrated nominal optical flat, and *vice versa*, in only one cryogenic cooldown? The proposition includes: a) interferometric phase-map measurements each with the test piece slightly offset in a different transverse Cartesian direction, and b), for synthesizing the 2-dimentional (2-D) wavefront distortion (WD), an unconventional numerical scheme starting with 1-dimentional (1-D) bi-direction integration. The numerical approach may help minimize the non-uniformity in integrated noise-power (NP) distribution that results from integrating data, and thus the associated uncorrelated random noise, from raw phase-maps. Herein, NP refers to the square of rms noise.

Upon cooling, optical-path lengths change. Consequently, it has been a challenge to perform interferometric optical-figure measurements at cryogenic temperatures. This is true even when measuring nominally flat optical components. One usually has to resort to assumptions, verifiable or not, making measurement results "interpretable" as well as questionable. In this type of measurements, one normally sets up the Fizeau interferometer mainframe at room temperature in front of the cryogenic dewar window

system. If the test piece were at room temperature, one would simply use a window system with its WD pre-calibrated with a reference flat that has a known room-temperature optical figure. The problem is in most cases such a calibrated reference flat is unavailable for the pertinent *cryogenic* temperature. In other words, one would start with either a cryogenically calibrated window system or a cryogenically calibrated reference flat. However, normally neither is available.

On the other hand, to calculate rather than directly measure the window-system WD, detailed information would be needed on the profiles of temperature, thermal-expansion coefficient (TEC), refractive index, mounting strain, etc. Unfortunately, these multivariate profiles are all difficult, if not impossible, to explore realistically. Of course, one might want to search for a reference flat with a sufficiently low TEC making the difference in optical figure negligibly small between room temperature and the cryogenic temperature of concern. However, it is extremely difficult to meet such requirements on TEC. For example, according to Reference 2, an exceptionally high quality fused quartz may have a spatial variation in TEC approximately equal to 20 ppb/K per cm as linearized over the range of [4, 300] K. Consequently, for a 15-cm diameter and 2.5-cm thick parallel reference flat made out of this material, the single-pass transmitted WD at 4 K could well be on the order of one wavelength in the visible, even if the flat were originally perfect at room temperature as far as its parallelism and refractive-index homogeneity are concerned. This implies that, to obtain an accuracy of $\lambda/20$ in measurement (where $\lambda = 633$ nm), one would need a TEC of ~1 ppb/K per cm, which is twenty times more demanding in comparison with what the state-of-the-art may provide.

To solve the problem, proposed is a straightforward scheme that may characterize the tilt-independent part of the WD due to the test piece as well as that due to the window system in only one cryogenic cooldown.

2. CONCEPT OF MEASUREMENT SCHEME

To set the stage, definitions and requirements are made as follows. x and y are the Cartesian coordinates in a plane perpendicular to the optical axis as determined by the interferometer. An implicit assumption is thus the optical axes of the inteferometer reference beam and the return beam from the test piece coincide with each other. The WDs due to the window system and the test piece are denoted as $W(x,y)$ and $T(x,y)$, respectively. For clarity, all WDs mentioned in the following are defined to be single-pass, unless stated otherwise. It is also required by the measurement scheme that

$$\{x \ \ domain \ \ of \ \ W(x,y)\} \supseteq \{x \ \ domain \ \ of \ \ T(x,y)\} \pm \Delta x \qquad (1)$$

and

$$\{y \ \ domain \ \ of \ \ W(x,y)\} \supseteq \{y \ \ domain \ \ of \ \ T(x,y)\} \pm \Delta y \qquad (2)$$

where Δx (> 0) and Δy (> 0) are the intended shifts of the test piece along the two transverse axes. Of course, one may define the domain for $T(x,y)$ through software such

that it meets the aforementioned requirements even if it is wider in area than the window. Therefore, the only physical requirement for the actual test piece is that there be enough clearance around it for lateral shifting.

The observed WD $Z(x,y)$ within the domain of $T(x,y)$ is then

$$Z(x,y) = W(x,y) + T(x,y) \tag{3}$$

by definition. On the other hand, the WD resulting from shifting the test piece, say, in the $+x$ direction by Δx becomes:

$$Z^{\Rightarrow}(x,y) = W(x,y) + T(x - \Delta x, y), \tag{4}$$

now within the new domain defined by the shifted test piece. Therefore, $Z(x,y) - Z^{\Rightarrow}(x,y)$, within the overlap region between the pre-shift and post-shift test piece domains, clearly provides information on the difference in $T(x,y)$ between two positions spaced by Δx. In principle, by measuring the WDs before and after shifting the test piece, for example, in both $+x$ and $+y$ direction, two sets of 1-D WDs due to the test piece become available, one set defined over grid segments parallel to the x axis and the other to the y axis. Apparently, these 1-D WDs are free of the window effect. This constitutes the basis of the proposed measurement scheme. The next step, as will be discussed later, is "weave" them together and derive the 2-D wavefront distortion function (WDF) for the test piece.

As a footnote, $Z^{\Rightarrow}(x+\Delta x, y) - Z(x,y)$ and $Z^{\Uparrow}(x, y+\Delta y) - Z(x,y)$ together certainly provide direct information on $W(x,y)$. However, because generally the test piece is of direct concern, the discussion will focus on deriving $T(x,y)$ instead. Nevertheless, $W(x,y)$ may still result as a by-product from $W(x,y) = Z(x,y) - T(x,y)$.

To simplify notation, it is further defined that $Z_{i,j} \equiv Z(i\Delta x, j\Delta y)$ with i, j being integers, and likewise for $W_{i,j}$, $T_{i,j}$, $Z^{\Rightarrow}_{i,j}$, $Z^{\Uparrow}_{i,j}$, etc. In other words, it is chosen to deal with WD values only at the Cartesian grid points. Of course, the concept of grid point is an idealization; in measurement, each grid point corresponds to a small neighboring and enclosing area over which the signal is averaged to generate the interferometric data to be associated with the grid point.

3. SYNTHESES OF 1-D FIGURES

Before synthesizing the 1-D WDFs, the effective domain of $T_{i,j}$ is to be determined to facilitate the subsequent synthesis of the 2-D WDF. This entails two further requirements.

The first is that every grid point $(i\Delta x, j\Delta y)$ be an intersection between the two corresponding orthogonal grid segments (labeled by j and i, respectively, for now) with each of them containing *two or more consecutive* such discrete intersections including the one of concern. This requirement eliminates some grid points around the edge(s) of the

original domain that is determined by the physical boundary (or boundaries) of the test piece, as exemplified in Figure 1. Consequently, associated with each $(i\Delta x, j\Delta y)$ inside the resulting domain, there are two functional values, namely, one from each of the two 1-D WDFs yet to be individually offset as a whole in z. This requirement is critical for an efficient synthesis of the 2-D WDF.

The first requirement may lead to multiple unconnected domains. The second requirement is thus that the domain of $T_{i,j}$ be topologically connected as one piece; only a *single* simply-connected, or multiply-connected, domain is involved at a time. This is consistent with the fact that, in interferometric figure measurements, the absolute phase difference between two separate domains is generally ambiguous.

The first requirement can be met by rastering scans in which one removes from the original test piece domain all grid points that have no immediate neighbors in the directions orthogonal to that of rastering. However, it takes three rastering scans, for example, first all in the $+x$ (or $-x$) direction, then in the $+y$ (or $-y$) direction, and finally in the $+x$ (or $-x$) direction *again*. As indicated in Figure 1, the third rastering scan is definitely not redundant.

Suppose, within the domain resulting from the aforementioned "deburring" process, there are n_x and n_y 1-D WDFs defined over grid segments *parallel* to the x axis and y axis, respectively. For clarity, each grid segment in the newly defined domain is

labeled with an integer s ranging from 1 through $n_x + n_y$, and the n_x segments parallel to the x axis are counted consecutively first.

The 1-D, and thus the 2-D, WDFs are to be synthesized under the assumption that the phase-map measurement noises at different grid points i) are *uncorrelated* and *random* in nature, and ii) share the same random NP. In other words, the NP per phase-map measurement per grid point is nominally constant from point to point and from map to map. Because NP is additive, creating a 1-D WDF with a uniform NP distribution would mean all points of the 1-D WDF are each a linear combination of the same *effective* number of raw data points obtained from the phase-map measurements. In here, the raw data points involved for each point of the 1-D WDF may not be the same set of raw data points. These statements apply to 2-D WDF as well.

To obtain the 1-D WDFs by integrating the difference data, the following conventional approach could be taken. For example, along a grid segment s parallel to the x axis,

$$T_{i,j}^{s} = \sum_{p=i_{\min}(s)+1}^{i} \left(Z_{p,j} - Z_{p,j}^{\Rightarrow} \right) \tag{5}$$

where $i_{\min}$ is the minimum integer coordinate along s. Unfortunately, Eq. (5) shows that the number of raw data points involved, i.e., $Z_{p,j}$ and $Z_{p,j}^{\Rightarrow}$, increases linearly with the

summation upper limit i; the NP resulting from integration depends on the integration coordinate. To solve the problem, a different scheme of numerical integration is devised:

$$T_{i,j}^{s}=\frac{1}{2}\sum_{p=i_{\min}(s)+1}^{i_{\max}(s)}\left[Sign\left(i-p+\frac{1}{2}\right)\left(Z_{p,j}-Z_{p,j}^{\Rightarrow}\right)\right] \tag{6}$$

where *Sign* is a function reflecting only the sign of its real argument, the value of 1/2 in the argument of *Sign* may be any number within open interval (0,1), $i_{\min}$ and $i_{\max}$ are the minimum and maximum integer coordinate along s. In a sense, Eq. (6) is the discrete version of

$$T(x,y)-\frac{1}{2}\left[T(x_{\min},y)+T(x_{\max},y)\right]=\frac{1}{2}\int_{x_{\min}}^{x_{\max}}Sign(x-\tau)\frac{\partial T(\tau,y)}{\partial\tau}d\tau, \tag{7}$$

with its right side corresponding to a *bidirectional* integration. Noticeably, the corresponding integration constant is ignored in Eq. (6) in that the "dc" component of the WD is of no significance for 1-D *per se*. Nevertheless, the optimal *relative* offsets among all derived 1-D WDFs will be determined later. As the foundation for the algorithm to be introduced, Eq. (6) features an NP distribution *independent* of the coordinate i along s because each $T_{i,j}^{s}$ for a specific s is a different linear combination of the *same* group of raw data points with coefficients being either 1 or -1. As a property,

the new numerical integration approach necessarily makes the integration interval, for example, $[i_{\min}(s)\Delta x, i_{\max}(s)\Delta x]$ in this case, embrace at least one zero-crossing point.

Although one may simply shift the test piece in only two directions, for example, in $+x$ and $+y$ as mentioned previously, the following discussion will focus on the four-shift measurement, which reflects the symmetry most dewar systems may provide. In other words, the test piece is shifted one at a time in the $+x$ and $-x$ direction by Δx, and similarly in the $+y$ and $-y$ direction by $\Delta y = \Delta x$. As a result, there are five wavefront measurements to deal with. Two new 1-D WDFs may accordingly be defined as:

$$T_{i,j}^{s\Leftrightarrow} \equiv \frac{1}{2}\left(T_{i,j}^{s\Leftarrow} + T_{i,j}^{s\Rightarrow}\right) \tag{8}$$

$$T_{i,j}^{s'\Updownarrow} \equiv \frac{1}{2}\left(T_{i,j}^{s'\Downarrow} + T_{i,j}^{s'\Uparrow}\right) \tag{9}$$

where

$$T_{i,j}^{s\Rightarrow} = \frac{1}{2}\sum_{m=i_{\min}(s)+1}^{i_{\max}(s)}\left[Sign\left(i-m+\frac{1}{2}\right)\left(Z_{m,j} - Z_{m,j}^{\Rightarrow}\right)\right], \tag{10}$$

$$T_{i,j}^{s\Leftarrow} = \frac{1}{2}\sum_{n=i_{\min}(s)}^{i_{\max}(s)-1}\left[Sign\left(i-n-\frac{1}{2}\right)\left(Z_{n,j}^{\Leftarrow} - Z_{n,j}\right)\right], \tag{11}$$

$$T_{i,j}^{s'\Uparrow} = \frac{1}{2} \sum_{p=j_{\min}(s')+1}^{j_{\max}(s')} \left[Sign\left(j - p + \frac{1}{2} \right) \left(Z_{i,p} - Z_{i,p}^{\Uparrow} \right) \right], \tag{12}$$

and

$$T_{i,j}^{s'\Downarrow} = \frac{1}{2} \sum_{q=j_{\min}(s')}^{j_{\max}(s')-1} \left[Sign\left(j - q - \frac{1}{2} \right) \left(Z_{i,q}^{\Downarrow} - Z_{i,q} \right) \right]. \tag{13}$$

$T^{s\Leftrightarrow}$ with $1 \le s \le n_x$ and $T^{s'\Updownarrow}$ with $n_x + 1 \le s' \le n_x + n_y$ thus represent two sets of experimentally derived 1-D WDFs. To be more specific, there are two values, i.e., $T_{i,j}^{s\Leftrightarrow}$ and $T_{i,j}^{s'\Updownarrow}$, associated with each grid point.

4. PRELIMINARY SYNTHESIS OF THE 2-D FIGURE

For synthesizing the 2-D WDF, one needs to determine the dc-offsets *among* all 1-D WDFs. Because there are two 1-D distortion values at each discrete location, the sum of squares of all such differences over the entire domain is to be minimized while each dc-independent 1-D distortion *figure* remains the same. In that there are still two values at every grid point after the minimization, one may then take the arithmetic average between the two as the experimentally derived value for the 2-D WDF at every grid point.

In the following, the minimization process is presented explicitly partly to provide a quick recipe for practical purposes but mainly to set the stage for a predictive noise analysis to be discussed in the next section. The minimization process is equivalent to solving the following set of simultaneous linear equations in c_s:

$$\frac{\partial}{\partial c_s}\sum_{i,j}\left|\left(T_{i,j}^{p\Leftrightarrow}+c_{p(i,j)}\right)-\left(T_{i,j}^{q\Updownarrow}+c_{q(i,j)}\right)\right|^2=0 \quad for\begin{cases} s=1,\ ...,\ n_x+n_y \\ p=1,\ ...,\ n_x \\ q=n_x+1,\ ...,n_x+n_y \end{cases} \tag{14}$$

where $c_{p(i,j)}$ and $c_{q(i,j)}$ are the two offset variables for the two grid segments p and q that intersect at $(i\Delta x, j\Delta y)$. It is noted that p and q are functions of $(i\Delta x, j\Delta y)$. From the *3-D perspective* formed by the two sets of 1-D WDFs defined over the two mutually orthogonal sets of 1-D domains, it is apparent that Eq. (14) has infinitely many sets of solutions. Certainly, it makes no difference if the whole set of c_s's is offset simultaneously by an arbitrary constant. This is consistent with the fact that the offset for the overall WDF is meaningless in terms of making optical-figure measurements. Therefore, one c_s needs to be fixed as a constant, or simply as zero for convenience. (The next section addresses the question of which one to fix.)

Eq. (14) can be rewritten in matrix form as

$$\hat{G}\overset{\downarrow}{C}=\overset{\downarrow}{F} \tag{15}$$

where $\hat{G}$ is a symmetric matrix, and $\vec{C}$ and $\vec{F}$ are column vectors. $\vec{C}$ consists of all $n_x + n_y$ of c_s's as variables to be determined. Again, the offsets for the grid segments parallel to the x axis are arranged to be the first n_x elements in $\vec{C}$. Accordingly, $\hat{G}$ becomes an $(n_x + n_y) \times (n_x + n_y)$ symmetric matrix characteristic of the geometry of the domain perimeter only. The elements of $\hat{G}$ are described as follows. One first establishes, for the upper-right corner of $\hat{G}$, an $n_x \times n_y$ sub-matrix $\hat{G}'$ with its elements $g'_{a,b}$ either equal to one if the grid segment a and the segment $n_x + b$ have an intersection, or equal to zero otherwise. Here, a ranges from 1 through n_x and b from 1 through n_y. One then sets the rest of the off-diagonal elements in the upper-right half of $\hat{G}$ to zeros. The diagonal elements of $\hat{G}$ are:

$$g_{s,s} = \begin{cases} -\sum_{p=1}^{n_y} g'_{s,p} & as \quad 1 \le s \le n_x \\ -\sum_{p=1}^{n_x} g'_{p,s-n_x} & as \quad n_x + 1 \le s \le n_x + n_y \end{cases} . \qquad (16)$$

Noticeably, it is as a result of the first domain requirement described in Section 3 that the sub-matrix $\hat{G}'$ contains all the information needed to generate $\hat{G}$. Based on Eqs. (8)-(13), the elements of $\vec{F}$ are

$$f_s = \begin{cases} \sum_{p=i_{\min}(s)}^{i_{\max}(s)} \left[T^{s\Leftrightarrow}_{p,j(p,s)} - T^{s'(p,j)\Updownarrow}_{p,j(p,s)} \right] \quad as \quad 1 \le s \le n_x \\ \sum_{p=j_{\min}(s)}^{j_{\max}(s)} \left[T^{s\Updownarrow}_{i(s,p),p} - T^{s'(i,p)\Leftrightarrow}_{i(s,p),p} \right] \quad as \quad n_x + 1 \le s \le n_x + n_y \end{cases} . \tag{17}$$

It is confirmed from the right side of Eq. (17) that the subscript s on the left completely determines the value of f_s.

To guarantee uniqueness in solution when the test piece domain is a *single* piece, the following set of simultaneous linear equations (in elements of the column vector $\overset{\downarrow}{C}^k$) can be solved instead

$$\hat{G}^k \overset{\downarrow}{C}^k = \overset{\downarrow}{F}^k \tag{18}$$

where $\hat{G}^k$ is the square matrix reduced from $\hat{G}$ by deleting the k th column and the k th row, and $\overset{\downarrow}{C}^k$ and $\overset{\downarrow}{F}^k$ are column vectors reduced from $\overset{\downarrow}{C}$ and $\overset{\downarrow}{F}$, respectively, by deleting their k th element. This is equivalent to implicitly setting c_k equal to zero or referencing all the other optimized offsets to the grid segment k as an "anchor." One may recall the zero-crossing property resulting from the bidirectional integration described in Section 3. Of course, trying to solve Eq. (18) also constitutes a test to see if the test piece domain is topologically connected. If it includes two or more pieces, then Eq. (18) would have no unique solution, or would result in no solution in *numerical* calculation.

5. SYNTHESIS OPTIMIZATION

The question of which c_k should be set to zero is essentially a noise issue. Resulting from the devised 1-D integration method, each 1-D WDF has a constant level of NP *within* its 1-D domain. However, the constant NP is proportional to the number of discrete points over that 1-D domain. Consequently, dependent on the overall 2-D domain geometry, the 2-D WDF resulting from Eq. (18) has generally a non-uniform NP distribution, whichever c_k has been set to zero.

For illustration only, provided here is a relative simple scenario (see Figure 2) in which a circular test piece covers eleven equally-spaced discrete points along both x and y axis, with $\Delta x = \Delta y$. The distribution of integrated NP can be derived as follows in unit of the average NP per grid-point per phase-map-measurement. Naturally, the experimentally-derived 2-D distortion for point $(i\Delta x, j\Delta y)$ may be defined as

$$T_{i,j} \equiv \frac{1}{2}\left[T_{i,j}^{a\Leftrightarrow} + c_a + T_{i,j}^{b\Updownarrow} + c_b\right]. \tag{19}$$

In view of Eqs. (8)-(13), and the solution of Eq. (18), each $T_{i,j}$ is thus a linear combination of $Z_{i',j'}$, $Z_{i',j'}^{\Rightarrow}$, $Z_{i',j'}^{\Leftarrow}$, $Z_{i',j'}^{\Uparrow}$, and $Z_{i',j'}^{\Downarrow}$ (to be collectively abbreviated as $Z_{i',j'}^{all}$s) with all pertinent i' and j'. Assume the average NPs associated with $Z_{i',j'}^{all}$s are all equal and independent of a) i' and j', and b) which phase-map measurement made as indicated by the superscripts "null," $\Rightarrow$, $\Uparrow$, etc. Then, for each grid point, the sum of all

coefficient-absolute-values of this linear combination becomes the estimated location-specific integrated NP. In other words, the integrated NP can be expressed in a unit such that its value is equivalent to the effective number of single phase-map measurements. Figure 2 shows two such derived distributions with each of them based on a different selection of the anchor-segment, as indicated by a pair of embracing arrows. Apparently, each distribution features a valley along the selected anchor-segment. Interestingly, such anchor-segment-specific NP distributions reflects a) a *convex* effect along the valley, and b) generally *concave* effects elsewhere.

A question to be addressed is how to minimize such non-uniformity as well as the maximum in integrated NP distribution, while essentially maintaining the same WD content of $T_{i,j}$ as would be obtained from a single phase-map measurement as if a single phase-map measurement were adequate to obtain $T_{i,j}$? A straightforward approach is average over all $n_x + n_y$ anchor-segment-specific 2-D WDFs. The associated NP distribution can be calculated as follows. For each grid point $(i\Delta x, j\Delta y)$, expand $T_{i,j}$ as a linear combination in $Z^{all}_{i',j'}$'s, as previously described. Then take the arithmetic average over all $n_x + n_y$ such anchor-segment-specific linear combinations for each discrete location. And finally sum over all the *coefficient-absolute-values* in the resultant expansion for each grid point to form the 2-D NP distribution. As a reminder, the estimation process is *not* the same as arithmetic-averaging over the $n_x + n_y$ 2-D NP distributions; the process is based on arithmetic-averaging over the $n_x + n_y$ anchor-segment-specific 2-D WDFs to begin with. Figure 3 shows such an NP distribution obtained for the same example case as for Figure 2. As expected, this averaging process

not only decreases the maximum and peak-to-valley value, but also erases the convex valley-like feature; generally speaking, it creates a concave distribution, or an edge-thickening effect. As a reference, Table 1 summarizes the resultant maximum and minimum NPs for circular test pieces with several low densities of grid points. For instance, Table 1 shows that if there are fifteen data points across the diameter along the x and the y axis, then, to decrease the maximum NP level of the synthesized 2-D WDF to less than the average noise level of a single phase-map measurement, one would need to *signal average* at least twelve phase maps for each of the five test-piece locations.

For simplicity in description, we name "each of the $n_x + n_y$ anchor-segment-specific optimizations" *Process a* (with *a* for anchor), "each complete set of $n_x + n_y$ Process a's" *Process A*, and "arithmetic-averaging over all $n_x + n_y$ anchor-segment-specific optimizations from Process A" *Process G*. In other words, Process A generates $n_x + n_y$ 2-D WDFs, which together may generate a single 2-D WDF through Process G. Now two counteracting effects have been observed in terms of curvature in NP distribution (*not* in WD). One is the convex effect along the anchor-segment from each Process a; the other is the global concave effect from Process G. These observations together suggest a potentially better optimization approach to further minimize the non-uniformity in integrated NP distribution. For example, from each initial Process a, one may a) single out the 1-D WDF along the selected anchor-segment from the resultant 2-D WDF, and then b) use all such 1-D WDFs as a set of inputs for another round of Process A. Hopefully, the second round of Process A may generate a new set of 1-D WDFs at the selected anchor-segments with even more convexities in NP distribution. In other words,

Process A may be iterated this way as many times as preferred. Such convexities resulting from each process A would then be ready for compensation by Process G. So to speak, after each Process A, Process G may serve as a check to see the effect on global non-uniformity in integrated NP distribution. In other words, one may set a minimization criterion for ending the entire iteration. A 2-D WDF may thus result free of any artifact valley and associated with a smaller non-uniformity in the integrated NP distribution.

The aforementioned iteration, however tedious it might seem, is perhaps needed only *once* for a) a given test-piece domain shape, and b) a given set of Cartesian grid points within, for us to explore the convergence behavior of the non-uniformity in integrated NP distribution. All the iteration generates is, on the one hand, for each grid point, an expression of $T_{i,j}$, namely, an optimized linear combination of $Z^{all}_{i',j'}$s, and, on the other hand, the associated NP distribution. A database for such linear-combination coefficients may certainly be created *prior to* measurement to determine the number of phase-map measurements to meet certain tolerance criteria on i) integrated NP non-uniformity, and ii) maximum NP.

As an important footnote, the finite shift steps, i.e., Δx and Δy, used in the proposed measurement scheme may lead to more useful data than have so far been discussed. Suppose, in terms of measurement, each grid point between orthogonal coordinate grid segments corresponds to a spot of a small finite area, say, approximately $\delta_x \delta_y$ where δ_x and δ_y are the area's approximate widths along the x and y direction, respectively. Because of the continuity nature of phase maps, the four-shift measurement

scheme, for instance, may lead to approximately as many as $4(\Delta x/\delta_x)(\Delta y/\delta_y)$ 2-D WDFs, which are overlapping and thus partially redundant and partially complementary. However, the question of how to make use of all such information is beyond the scope of the article, and will be addressed separately in the future.

6 REMARKS ON TESTING & IMPLIMENTATION

One would typically deal with data-point densities of approximately thirty points across the test-piece diameter in measuring the corresponding low-order Zernike components of the figure. "For definition of Zernike components, see Reference 3." In this case to achieve an average noise level less than that of a single phase-map measurement, one would, as extrapolating from Table 1, expect to signal-average over approximately twenty phase maps for each of the five laterally offset locations of the test piece. The optical and mechanical stability that would be required over the time needed for completing all five signal-averagings were demonstrated under cryogenic conditions according to Reference 2; the WD and associated noise level resulting from a single phase-map measurement did not noticeably vary over twenty hours, i.e., a time scale orders-of-magnitude exceeding the requirement of concern.

In case an unusually high density of data points is required, one could alternatively take an incremental approach in shifting the test piece. For example, start with a relatively large shift step to ensure a low noise level resulting from the 2-D figure synthesis. Then repeat the same scheme with a shift step, say, half of the initial one. In

other words, it is first established a low-density and thus low-noise figure framework, which also subdivides the figure into smaller regions. Because one may synthesize these smaller regions individually in a similar manner with a smaller shift step, the remaining question is simply: how to concatenate them together appropriately? It is a question that can certainly be addressed through a variety of software approaches.

The verification through hardware may comprise two parts as follows: (1) verification of the data-reduction software by conducting room-temperature measurements, and (2) end-to-end verification using cryogenic setups. For room-temperature verification, one can use two different experimental configurations, which may be denoted as F/W/T and F/T where F, W, and T represent Fizeau interferometer mainframe, window system, and test piece, respectively, following the order of physical arrangement. Of course, the test piece in the two configurations has to be the same such that one may compare the test-piece figures obtained from the two experimental configurations. Similarly, for the cryogenic end-to-end verification one may use two other configurations, which can be denoted as F/W/T_1 and F/W/T_2 where T_1 and T_2 represent two circular test pieces of the same diameter. Basically, T_1 and T_2 are mounted, inside the cryogenic dewar, on the same X-Y stage supported by a rotation stage, by which their locations can be interchanged. In this case, if W covers both T_1 and T_2, one may compare the window transmission figures before and after the interchange to verify the scheme. Similarly, one may also compare the figures of T_1 (or T_2) before and after the interchange. The results of such testing and implementation through hardware will be presented in a separate future article.

7 CONCLUDING REMARKS

It is proposed that the catch-22 loop in simultaneously measuring individual wavefront distortions of two in-series optical elements can be resolved by a simple approach, namely, additionally measuring the net wavefront distortions each resulting from the two elements *offset* in one of the four Cartesian directions perpendicular to the optical axis. The type of interferometry employed is unlimited to Fizeau, which however is typical and perhaps most convenient in a cryogenic measurement scenario as given in the article. For minimizing non-uniformity in integrated uncorrelated random-noise power in the resulting wavefront distortions, the proposed non-Newtonian numerical integration scheme is specific of the effective test-piece domain shape. Such numerical integration scheme for combining the net wavefront distortion data may be determined algorithmically *prior* to measurement according to criteria on noise-level tolerance; its determination thus poses no concern about computer speed in the corresponding real-time wavefront synthesis. The domain-shape-specific integration scheme *per se* represents a new and general numerical concept for integrating noise-carrying *experimental* data. Its generalization for higher dimensional data sets is conceivably feasible.

ACKNOLEDGEMENTS

The author wishes to thank C. W. F. Everitt, J. Turneaure, and J. Lipa at Stanford University for their support in conducting the research, and Bruce Warner at LLNL for

his support in preparing the manuscript. This work was funded mainly by NASA Contract # NAS8-36125, and partly by the LLNL NIF program.

REFERENCES

1. M. V. Mantravadi, "Newton, Fizeau, and Haidinger Interferometers," Chap. 1 in *Optical Shop Testing*, 2nd ed., D. Malacara Ed., pp. 18-35, John Wiley & Sons, New York, NY (1991).
2. D. H. Gwo, S. Wang, K. A. Bower, L. Huff, and J. A. Lipa, The NASA/Stanford Gravity Probe B Relativity Mission, private communication (1996).
3. D. Malacara and S. L. DeVore, "Interferogram Evaluation and Wavefront Fitting," Chap. 13 in *Optical Shop Testing*, 2nd ed., D. Malacara Ed., pp. 455-500, John Wiley & Sons, New York, NY (1991).

BIOGRAPHY

Dz-Hung Gwo earned his B.Sc. in chemistry from the National Tsing Hua University in Taiwan in 1980, and Ph.D. in chemistry/molecular physics from the University of California at Berkeley in 1989. His Ph.D. work was mostly related to high-resolution far-infrared spectroscopy on van der Waals clusters. He made the first theoretical prediction on the existence of unique-Q-branch vibrational-band patterns due to intra-molecular poly-proton tunneling motions. He then joined the staff of the NASA/Stanford Gravity Probe B (GPB) Relativity Mission at Stanford University to develop the cryogenic guide-

star-pointing system for the GPB satellite science probe. Currently he is a research physicist at the Lawrence Livermore National Laboratory.

This work was performed under the auspices of the U. S. Department of Energy by University of California, Lawrence Livermore National Laboratory under contract W-7405-Eng-48.

TABLE(S)

Table 1 Resulting from one iteration of Process A and then Process G (both defined in Section 5), the maximum and minimum noise powers for circular test pieces with several low densities of discrete points arranged in the Cartesian manner. The noise powers are in unit of the average noise power per phase-map measurement per discrete point, under the assumption the phase-map measurement noises at different discrete points i) are *uncorrelated* and *random* in nature, and ii) share the same random noise power. So to speak, the noise power per phase-map measurement per discrete point is a constant from point to point.

Number of discrete points across the diameter along the x, or y, axis	5	7	9	11	13	15
Maximum noise power	2.8	4.9	6.5	8.6	10.2	11.8
Minimum noise power	2.7	4.2	5.4	7.0	8.2	9.3

LIST OF FIGURE CAPTIONS

Figure 1 An illustration of the domain-defining process. Discrete locations represented by characters other than "–" are within the boundary of the effective pre-shift test piece. Locations represented by "–" are outside the boundary. Suppose we conduct rastering elimination first in the $+x$ direction from top to bottom, then in the $-y$ direction from left to right, and finally in the $+x$ direction again from top down. Character D's indicate the resulting domain to be used in the reduction scheme. Other characters represent locations eliminated in different steps. For example, $X3$ refers to a point eliminated in the third rastering elimination, which is in the $+x$ direction.

Figure 2 Two noise-power distributions, (a) and (b), resulting from different anchor-segment selections in Process a, as defined in Section 5. In this particular example, we consider a circular test piece, whose boundary encloses all discrete points labeled by either a number representing the calculated noise power or a character "E". The noise powers are in unit of the average noise power per phase-map measurement per discrete point, under the assumption the phase-map measurement noises at different discrete points i) are *uncorrelated* and *random* in nature, and ii) share the same random noise power. So to speak, the noise power per phase-map measurement per discrete point is a constant from point to point. "E" denotes a point eliminated in the domain-defining process. Arrows indicate the anchor-segment locations used in Process a.

Figure 3 An illustration of the noise-power distribution from one round of Process G, as defined in Section 5. (Refer to the caption of Figure 2 for notations and assumptions.)

FIGURE 1

(For Editor's information, Figures 1, 2(a), 2(b), and 3 are generated using the Microsoft Equation Editor in WORD; they are not normal line art. Therefore, they are not put in the TIFF or other suggested formats; they are attached as part of the text for optimal ***resolution and scalability***.)

–	–	$Y2$	–	$Y2$	–	–	–	–	$Y2$	–	–
–	$X1$	$Y2$	–	D	D	–	–	$X3$	$X3$	$X3$	–
–	–	D	D	D	D	D	–	$Y2$	–	$Y2$	–
$X1$	$X1$	D	D	D	D	D	D	D	$X1$	$Y2$	–
–	–	–	D	D	D	D	D	D	–	–	–
–	–	–	D	D	–	D	D	–	–	–	–
–	–	–	–	D	D	D	D	–	–	–	–
–	–	–	–	D	D	–	D	D	–	–	–
–	–	–	–	$Y2$	–	$Y2$	–	D	D	–	–
–	–	–	–	$Y2$	$X1$	$Y2$	–	D	D	D	–
–	–	–	–	–	–	–	–	–	D	D	–
–	–	–	–	–	–	–	–	–	–	–	–

FIGURE 2(a)

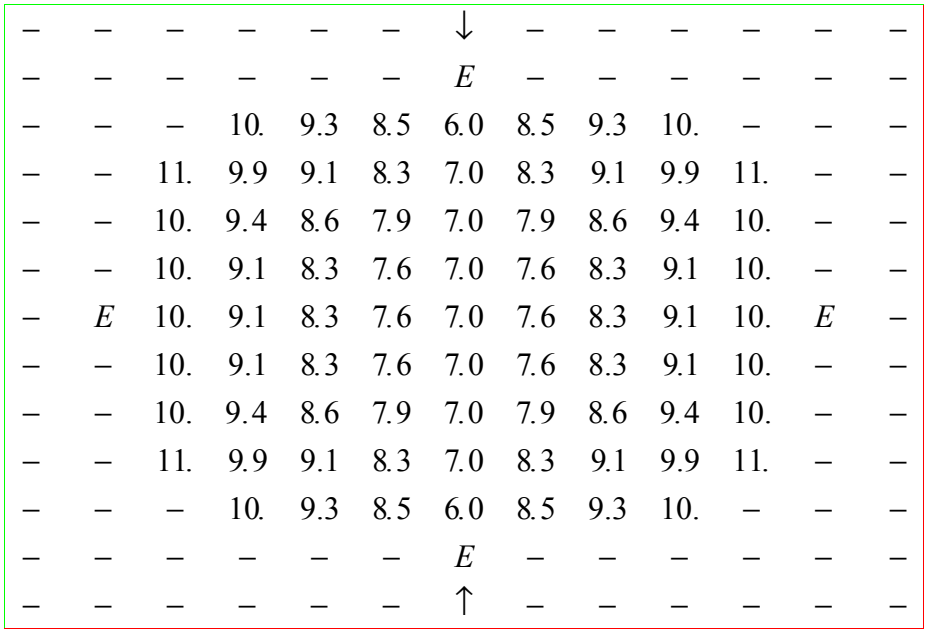
– – – – – – ↓ – – – – – –
– – – – – – E – – – – – –
– – – 10. 9.3 8.5 6.0 8.5 9.3 10. – – –
– – 11. 9.9 9.1 8.3 7.0 8.3 9.1 9.9 11. – –
– – 10. 9.4 8.6 7.9 7.0 7.9 8.6 9.4 10. – –
– – 10. 9.1 8.3 7.6 7.0 7.6 8.3 9.1 10. – –
– E 10. 9.1 8.3 7.6 7.0 7.6 8.3 9.1 10. E –
– – 10. 9.1 8.3 7.6 7.0 7.6 8.3 9.1 10. – –
– – 10. 9.4 8.6 7.9 7.0 7.9 8.6 9.4 10. – –
– – 11. 9.9 9.1 8.3 7.0 8.3 9.1 9.9 11. – –
– – – 10. 9.3 8.5 6.0 8.5 9.3 10. – – –
– – – – – – E – – – – – –
– – – – – – ↑ – – – – – –

(a)

FIGURE 2(b)

–	–	–	–	–	–	–	–	–	–	–	–	–
–	–	–	–	–	–	*E*	–	–	–	–	–	–
–	–	↓	11.	11.	11.	11.	12.	13.	13.	–	–	–
–	–	6.9	9.5	9.6	9.9	10.	11.	12.	12.	13.	–	–
–	–	7.4	8.9	9.0	9.3	9.7	10.	11.	12.	12.	–	–
–	–	7.4	8.5	8.7	9.0	9.4	9.9	11.	11.	12.	–	–
–	*E*	7.4	8.4	8.6	8.9	9.3	9.8	11.	11.	12.	*E*	–
–	–	7.4	8.5	8.7	9.0	9.4	9.9	11.	11.	12.	–	–
–	–	7.4	8.9	9.0	9.3	9.7	10.	11.	12.	12.	–	–
–	–	6.9	9.5	9.6	9.9	10.	11.	12.	12.	13.	–	–
–	–	↑	11.	11.	11.	11.	12.	12.	13.	–	–	–
–	–	–	–	–	–	*E*	–	–	–	–	–	–
–	–	–	–	–	–	–	–	–	–	–	–	–

(b)

FIGURE 3

–	–	–	–	–	–	–	–	–	–	–	–	–
–	–	–	–	–	–	*E*	–	–	–	–	–	–
–	–	–	8.6	8.3	8.2	8.1	8.2	8.3	8.6	–	–	–
–	–	8.6	8.0	7.7	7.6	7.5	7.6	7.7	8.0	8.6	–	–
–	–	8.3	7.7	7.4	7.3	7.2	7.3	7.4	7.7	8.3	–	–
–	–	8.2	7.6	7.3	7.1	7.1	7.1	7.3	7.6	8.2	–	–
–	*E*	8.1	7.5	7.2	7.1	7.0	7.1	7.2	7.5	8.1	*E*	–
–	–	8.2	7.6	7.3	7.1	7.1	7.1	7.3	7.6	8.2	–	–
–	–	8.3	7.7	7.4	7.3	7.2	7.3	7.4	7.7	8.3	–	–
–	–	8.6	8.0	7.7	7.6	7.5	7.6	7.7	8.0	8.6	–	–
–	–	–	8.6	8.3	8.2	8.1	8.2	8.3	8.6	–	–	–
–	–	–	–	–	–	*E*	–	–	–	–	–	–
–	–	–	–	–	–	–	–	–	–	–	–	–